The Astrophysical Journal, 835:131 (8pp), 2017 February 1 doi:10.3847/1538-4357/835/2/131

PTF1 J082340.04+081936.5: A Hot Subdwarf B Star with a Low-mass White Dwarf Companion in an 87-minute Orbit

Thomas Kupfer[1], Jan van Roestel[2], Jared Brooks[3], Stephan Geier[4], Tom R. Marsh[5], Paul J. Groot[2], Steven Bloemen[2], Thomas A. Prince[1], Eric Bellm[1], Ulrich Heber[6], Lars Bildsten[3,7], Adam A. Miller[8,9], Martin J. Dyer[10], Vik S. Dhillon[10,11], Matthew Green[5], Puji Irawati[12], Russ Laher[13], Stuart P. Littlefair[10], David L. Shupe[14], Charles C. Steidel[1], Somsawat Rattansoon[10,12], and Max Pettini[15]

[1] Division of Physics, Mathematics and Astronomy, California Institute of Technology, Pasadena, CA 91125, USA; tkupfer@caltech.edu
[2] Department of Astrophysics/IMAPP, Radboud University Nijmegen, P.O. Box 9010, NL-6500 GL Nijmegen, The Netherlands
[3] Department of Physics, University of California, Santa Barbara, CA 93106, USA
[4] Institute for Astronomy and Astrophysics, Kepler Center for Astro and Particle Physics, Eberhard Karls University, Sand 1, D-72076 Tübingen, Germany
[5] Department of Physics, University of Warwick, Coventry CV4 7AL, UK
[6] Dr. Remeis-Sternwarte and ECAP, Astronomical Institute, University of Erlangen-Nuremberg, Germany
[7] Kavli Institute for Theoretical Physics, Santa Barbara, CA 93106, USA
[8] Center for Interdisciplinary Exploration and Research in Astrophysics (CIERA) and Department of Physics and Astronomy, Northwestern University, 2145 Sheridan Road, Evanston, IL 60208, USA
[9] The Adler Planetarium, 1300 S. Lakeshore Drive, Chicago, IL 60605, USA
[10] Department of Physics and Astronomy, University of Sheffield, Sheffield, S3 7RH, UK
[11] Instituto de Astrofsica de Canarias (IAC), E-38200 La Laguna, Tenerife, Spain
[12] National Astronomical Research Institute of Thailand, 191 Siriphanich Building, Huay Kaew Road, Chiang Mai 50200, Thailand
[13] Spitzer Science Center, California Institute of Technology, Pasadena, CA 91125, USA
[14] Infrared Processing and Analysis Center, California Institute of Technology, Pasadena, CA 91125, USA
[15] Institute of Astronomy, Madingley Road, Cambridge CB3 0HA, UK

Received 2016 November 14; revised 2016 December 5; accepted 2016 December 6; published 2017 January 23

Abstract

We present the discovery of the hot subdwarf B star (sdB) binary PTF1 J082340.04+081936.5. The system has an orbital period of $P_{\rm orb} = 87.49668(1)$ minutes (0.060761584(10) days), making it the second-most compact sdB binary known. The light curve shows ellipsoidal variations. Under the assumption that the sdB primary is synchronized with the orbit, we find a mass of $M_{\rm sdB} = 0.45^{+0.09}_{-0.07}\ M_{\odot}$, a companion white dwarf mass of $M_{\rm WD} = 0.46^{+0.12}_{-0.09}\ M_{\odot}$, and a mass ratio of $q = \frac{M_{\rm WD}}{M_{\rm sdB}} = 1.03^{+0.10}_{-0.08}$. The future evolution was calculated using the MESA stellar evolution code. Adopting a canonical sdB mass of $M_{\rm sdB} = 0.47\ M_{\odot}$, we find that the sdB still burns helium at the time it will fill its Roche lobe if the orbital period was less than 106 minutes at the exit from the last common envelope (CE) phase. For longer CE exit periods, the sdB will have stopped burning helium and turned into a C/O white dwarf at the time of contact. Comparing the spectroscopically derived $\log g$ and $T_{\rm eff}$ with our MESA models, we find that an sdB model with a hydrogen envelope mass of $5 \times 10^{-4}\ M_{\odot}$ matches the measurements at a post-CE age of 94 Myr, corresponding to a post-CE orbital period of 109 minutes, which is close to the limit to start accretion while the sdB is still burning helium.

Key words: binaries: close – stars: individual (PTF1 J082340.04+081936.5) – subdwarfs – white dwarfs

1. Introduction

Hot subdwarf B stars (sdBs) are core helium burning stars with masses of around 0.5 $M_{\odot}$ and thin hydrogen envelopes (Heber 1986, 2009, 2016). A large fraction of sdBs are members of short-period binaries with periods below ≈10 days (Maxted et al. 2001; Napiwotzki et al. 2004). Orbital shrinkage through a common envelope (CE) phase is the only likely formation channel for such short-period sdB binaries (Han et al. 2002, 2003).

Evolutionary studies have shown that the orbital period of a hot subdwarf with a white dwarf companion has to be $P_{\rm orb} \lesssim 120$ minutes on exit from the last CE to still have an sdB that is core or shell helium burning when it fills its Roche lobe assuming that the further orbital period evolution is set by the emission of gravitational waves only. In the subsequent evolution, if helium burning is still ongoing, the sdB fills its Roche lobe first and starts to transfer He-rich material onto the white dwarf (e.g., Tutukov & Fedorova 1989; Tutukov & Yungelson 1990; Iben & Tutukov 1991; Yungelson 2008). If the system has a mass ratio of $q = M_{\rm sdB}/M_{\rm WD} \lesssim 2$, stable mass transfer is possible (Savonije et al. 1986; Wang et al. 2009). Mass transfer starts at orbital periods ranging from 16 to 50 minutes. Subsequently, the semi-detached system evolves to shorter periods with typical mass-transfer rates of $\dot{M} \approx 10^{-8}\ M_{\odot}\ {\rm yr}^{-1}$ (e.g., Savonije et al. 1986; Yungelson 2008; Piersanti et al. 2014; Brooks et al. 2015).

CD−30° 11223 has the shortest known orbital period of all sdB binaries ($P_{\rm orb} = 70.52986$ minutes) and is the only known system where the sdB is still expected to be burning helium when it will fill its Roche lobe (Vennes et al. 2012; Geier et al. 2013). After accreting 0.1 $M_{\odot}$, He burning is predicted to be ignited unstably in the accreted helium layer. This in turn triggers the ignition of carbon in the core, which might disrupt the WD even when the mass is significantly below the Chandrasekhar mass (e.g., Livne 1990; Livne & Arnett 1995; Fink et al. 2010; Woosley & Kasen 2011; Geier et al. 2013; Shen & Bildsten 2014). If the WD is not disrupted, the unstable burning of the He-shell will detonate the shell and may be observed as a faint and fast Ia supernova (Bildsten et al. 2007). This increases the orbital separation, but gravitational wave

radiation drives the donor back into contact, resuming mass transfer and triggering several subsequent weaker flashes (Brooks et al. 2015).

Inspired by the discovery of CD−30° 11223, we have conducted a search for (ultra-)compact post-CE systems using the Palomar Transient Factory (PTF; Law et al. 2009; Rau et al. 2009) large area synoptic survey based on a color selected sample from the Sloan Digital Sky Survey (SDSS). The PTF uses the Palomar 48″ Samuel Oschin Schmidt telescope to image up to ≈2000 deg^2 of the sky per night to a depth of $R_{\rm mould} \approx 20.6$ mag or $g' \approx 21.3$ mag. Here we report the discovery of the ultracompact sdB+WD system PTF1 J082340.04+081936.5 (hereafter PTF1 J0823). PTF1 J0823 has the second shortest orbital period among the known binaries with a hot subdwarf component.

2. Observations and Data Reduction

2.1. Photometry

As part of the PTF, the Palomar 48 inch (P48) telescope images the sky every night. The reduction pipeline for PTF applies standard de-biasing, flat fielding, and astrometric calibration to raw images (Laher et al. 2014). Relative photometry correction is applied and absolute photometric calibration to the few percent level is performed using a fit to SDSS fields observed in the same night (Ofek et al. 2012). The light curve of PTF1 J0823 has 144 epochs with good photometry in the $R_{\rm mould}$ band with a typical uncertainty of 0.01 mag. The cadence is highly irregular, ranging from 10 minutes to years with an average separation of about 10 days.

High cadence observations were conducted using the 2.4 m Thai National Telescope (TNT) with the high-speed photometer ULTRASPEC (Dhillon et al. 2014). ULTRASPEC employs a 1024 × 1024 pixel frame-transfer, electron-multiplying CCD in conjunction with re-imaging optics to image a field of 7.′7 × 7.′7 at (windowed) frame rates of up to ∼200 Hz. Observations were obtained with the g' filter on 2016 January 31 over 1 hr 50 minutes with an exposure time of 3.9 s and a dead time of 15 ms leading to a total of 2404 epochs. Data reduction was carried out with the ULTRACAM pipeline (Dhillon et al. 2007). All frames were bias-subtracted and flat fielded.

2.2. Spectroscopy

Optical spectra of PTF1 J0823 were obtained with the Palomar 200 inch telescope and the Double-Beam Spectrograph (DBSP; Oke & Gunn 1982) over three nights using a low resolution mode ($R \sim 1500$). We took seven consecutive exposures on 2015 October 25, 16 exposures on 2016 January 30, and 20 exposures on 2016 February 2 all with an exposure time of 240 s. Each night, an average bias frame was made out of 10 individual bias frames and a normalized flat-field frame was constructed out of 10 individual lamp flat fields. For the blue arm, FeAr and for the red arm, HeNeAr arc exposures were taken in the beginning and end of the night. Each exposure was wavelength calibrated by interpolating between the beginning and end of the night calibration exposures. Both arms of the spectrograph were reduced using a custom `PyRAF`-based pipeline[16] (Bellm & Sesar 2016). The pipeline performs standard image processing and spectral reduction procedures, including bias subtraction, flat-field correction, wavelength calibration, optimal spectral extraction, and flux calibration.

On 2016 April 13, we obtained 12 consecutive spectra using the William Herschel Telescope (WHT) and the ISIS spectrograph (Carter et al. 1993) using a medium resolution mode (R600B grating, $R \approx 3000$). One hundred bias frames were obtained to construct an average bias frame and 100 individual tungsten lamp flat fields were obtained to construct a normalized flat-field. CuNeAr arc exposures were taken before and after the observing sequence as well as after six spectra to correct for instrumental flexure. Each exposure was wavelength calibrated by interpolating between the two closest calibration exposures. All spectra were de-biased and flat fielded using `IRAF` routines. One-dimensional spectra were extracted using optimal extraction and were subsequently wavelength and flux calibrated.

Additionally, PTF1 J0823 was also observed on 2016 March 1 using Keck with the HIRES spectrograph ($R \approx 36{,}000$). The full data set consists of six spectra, which were taken consecutively. ThAr arc exposures were taken at the beginning of the night. The spectra were reduced using the `MAKEE`[17] pipeline following the standard procedure: bias subtraction, flat fielding, sky subtraction, order extraction, and wavelength calibration.

Table 1 gives an overview of all observations and the instrumental set-ups.

3. Orbital and Atmospheric Parameters

The dominant variation in the light curve is due to the ellipsoidal deformation of the sdB primary. This is caused by the tidal influence of the compact companion. The light curve also shows Doppler boosting, caused by the orbital motion of the sdB (Shakura & Postnov 1987; Bloemen et al. 2011; Geier et al. 2013). The ephemeris has been derived from the PTF light curve using the `Gatspy` module for time series analysis, which uses the Lomb-Scargle periodogram[18] (VanderPlas & Ivezić 2015). Because of the timebase of more than five years, the derived orbital period of $P_{\rm orb} = 87.49668(1)$ minutes (0.060761584(10) days) is accurate to 1 ms. The error was estimated by bootstrapping the data.

To obtain radial velocities, we followed the procedure as described in detail in Geier et al. (2011). To fit the continuum, line and line core of the individual lines we fitted Gaussians, Lorentzians, and polynomials to the hydrogen and helium lines using the `FITSB2` routine (Napiwotzki et al. 2004). The wavelength shifts compared to the rest wavelengths of all suitable spectral lines were fitted simultaneously using a χ^2-minimization. We found consistent velocities between the six HIRES spectra and the ISIS spectra taken at the same orbital phase, as well as consistent velocity amplitudes between the ISIS and DBSP spectra. However, we found a significant offset of the systematic velocities between the DBSP and the ISIS spectra. In the night of 2016 January 30 the systemic velocity of the DBSP spectra was shifted by 50 km s^{-1}. The DBSP calibration spectra were taken at the beginning and end of the night. For ISIS, the calibration lamps were taken at the position of the target before, after, and during the sequence and the velocities from the HIRES spectra are consistent with the

[16] https://github.com/ebellm/pyraf-dbsp

[17] http://www.astro.caltech.edu/~tb/ipac_staff/tab/makee/

[18] http://dx.doi.org/10.5281/zenodo.14833

Table 1
Summary of the Observations of PTF1 J0823

Date	UT	Tele./Inst.	N_{exp}	Exp. Time (s)	Coverage (Å)/Filter
Photometry					
2009 Nov 16–2015 Jan 15		Palomar 48 inch	144	60	R_{mould}
2016 Jan 31	14:10–16:50	TNT/ULTRASPEC	2404	3.94	g'
Spectroscopy					
2015 Oct 25	11:30–12:00	200 inch/DBSP	7	240	3800–10,000
2016 Jan 30	07:04–07:52	200 inch/DBSP	16	240	3800–10,000
	09:42–10:03				
2016 Feb 03	06:59–08:26	200 inch/DBSP	20	240	3800–10,000
2016 Mar 01	05:46–06:07	Keck/HIRES	6	180	3700–5000
2016 Apr 13	20:18–21:21	WHT/ISIS	12	290	3700–7400

ISIS spectra. Therefore, we conclude that the offset in the DBSP spectra is due to instrumental flexure because the calibration lamps were not taken at the position of the object. We corrected the velocities measured in the DBSP spectra to fit the systemic velocity obtained by the ISIS spectra. All velocities were folded on the ephemeris, which was derived from the photometric data. Assuming circular orbits, a sine curve was fitted to the folded radial velocity (RV) data points. We find a semi-amplitude $K = 211.7 \pm 1.8$ km s^{-1} and a systemic velocity of $\gamma = 33.3 \pm 1.4$ km s^{-1} (Figure 1).

The atmospheric parameters of effective temperature, $T_{\rm eff}$, surface gravity, $\log g$, helium abundance, $\log y$, and projected rotational velocity, $v_{\rm rot} \sin i$, were determined by fitting the rest-wavelength corrected average DBSP, ISIS, and HIRES spectra with metal-line-blanketed LTE model spectra (Heber et al. 2000). The most sensitive lines for $\log g$ and $T_{\rm eff}$ are the Balmer lines close to the Balmer jump. We used the hydrogen lines H12 (3750 Å) up to Hβ in the WHT/ISIS spectrum to measure $T_{\rm eff}$ and $\log g$ with $v_{\rm rot} \sin i$ as a free parameter and found $T_{\rm eff} = 27{,}100 \pm 500$ K, $\log g = 5.50 \pm 0.05$, and $v_{\rm rot} \sin i = 122 \pm 21$ km s^{-1} (Figure 2). The HIRES spectra are not well suited to measure $T_{\rm eff}$ and $\log g$ because the broad hydrogen absorption lines span several orders and merging of the echelle spectra could introduce systematic errors. However, the high-resolution HIRES spectra are well suited to measure the projected rotational velocity $v_{\rm rot} \sin i$ of the sdB in lines, which are not affected by order merging. The three helium lines (4026, 4471, 4921 Å), which are covered by the HIRES spectrum and not affected by order merging are less sensitive to $T_{\rm eff}$ and $\log g$, and most sensitive to rotational broadening $v_{\rm rot} \sin i$ and the helium abundance $\log y$. Therefore, they were used to measure $\log y$ and $v_{\rm rot} \sin i$, keeping $T_{\rm eff}$ and $\log g$ fixed to the values measured from the ISIS spectra. We found $v_{\rm rot} \sin i = 132 \pm 5$ km s^{-1} and $\log y = -2.47 \pm 0.03$ (Figure 3). As a consistency check $T_{\rm eff}$ and $\log g$ were derived from the DBSP spectrum keeping $\log y$ and $v_{\rm rot} \sin i$ fixed to the values measured from HIRES. Although, the DBSP spectrum only covers hydrogen lines down to H9 (3835 Å) we find good agreement within the errors with the parameters derived from the ISIS spectra. However, because of the larger coverage of Balmer lines, the further analysis will be done using $T_{\rm eff}$ and $\log g$ from the ISIS spectra.

Table 2 shows the atmospheric parameters and Table 3 summarizes the orbital parameters.

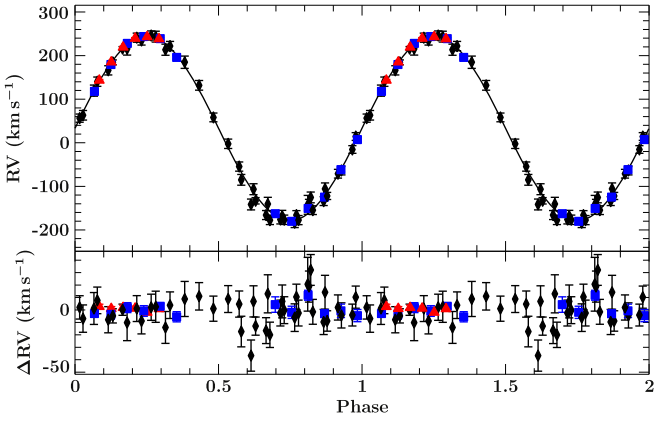

Figure 1. Radial velocity plotted against orbital phase. The RV data were phase folded with the orbital period and are plotted twice for better visualization. The residuals are plotted below. The RVs were measured from spectra obtained with P200/DBSP (black diamonds), WHT/ISIS (blue squares), and Keck/HIRES (red triangles).

4. Light Curve Analysis

To model the light curve, we used the LCURVE code (Copperwheat et al. 2010). LCURVE uses many points in a grid to model the surfaces of the stars with a shape according to the Roche geometry. We assume co-rotation and an eccentricity of zero. The flux that each point on the grid emits is calculated by assuming a blackbody of a certain temperature at the bandpass wavelength, corrected for limb darkening, gravity darkening, Doppler beaming, and the reflection effect.

We use information from spectroscopy and the P48 light curve to fix or constrain some of the model parameters. First, we fix the orbital period to the value as determined in Section 3. Second, we fix the primary temperature ($T_{\rm eff}$), primary RV amplitude (K), the surface gravity of the primary (g), and the rotational velocity ($v_{\rm rot} \sin i$, see Section 3). As an additional constraint, we use as a lower limit for the white dwarf radius the zero-temperature mass radius relation by Eggleton (quoted from Verbunt & Rappaport 1988). We use the same method to account for limb darkening and gravity darkening as described in Bloemen et al. (2011): the Claret limb darkening prescription from Claret (2004) and the gravity darkening prescription from von Zeipel (1924) with a passband specific gravity darkening coefficient. We investigated how the limb darkening coefficient affects the results by adding it as a free parameter with $\beta = 0.1 - 1.0$. The co-variance between the limb darkening parameter and system parameters is negligible compared to the uncertainty on the parameters. Therefore, we kept the limb

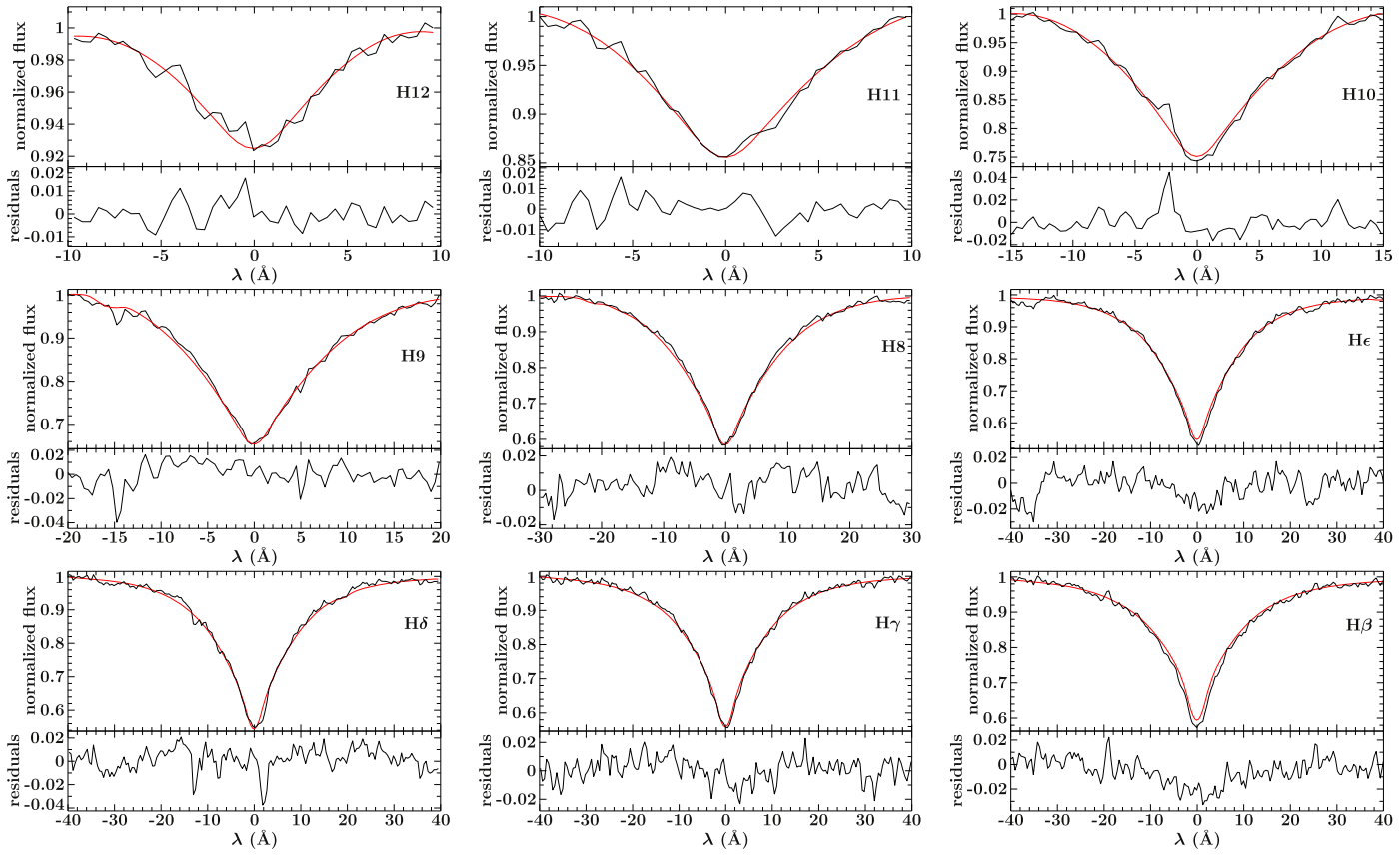

Figure 2. Fit of synthetic LTE models to the hydrogen Balmer lines of a coadded ISIS spectrum. The normalized fluxes of the single lines are shifted for better visualization.

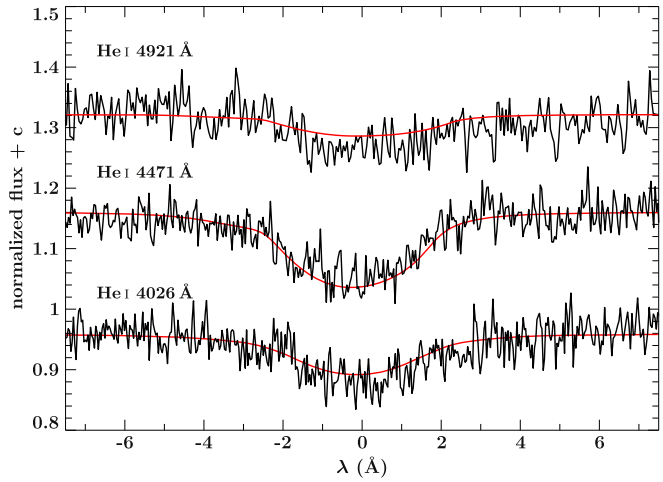

Figure 3. Best fits of $v_{\rm rot} \sin i$ to the helium lines seen in the HIRES spectra. The atmospheric parameters were fixed to the values derived from the WHT spectra.

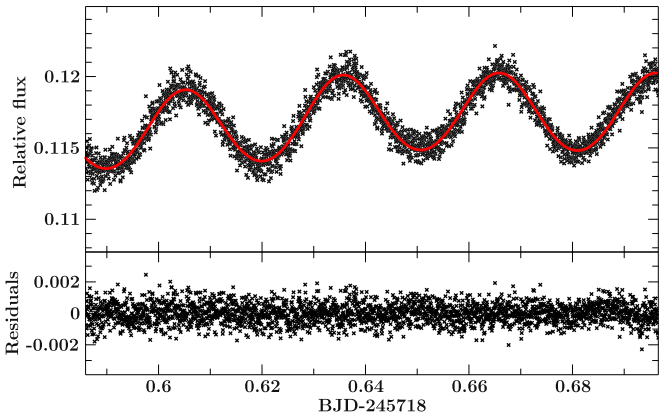

Figure 4. Light curve obtained with ULTRASPEC shown together with the `Lcurve` fit. The residuals are plotted below.

darkening coefficients fixed for the analysis. The limb darkening coefficients are $a_1 = 0.677$, $a_2 = -0.312$, $a_3 = 0.212$, and $a_4 = -0.079$ for the limb darkening coefficient $\beta = 0.460$. These values are calculated for an sdB with a temperature of $T_{\rm eff} = 27{,}100$ K and $\log g = 5.50$ using the models from Bloemen et al. (2011). We did not use any limb darkening or gravity darkening in the white dwarf model since these do not affect the light curve. This leaves as free parameters in the model the mass ratio q, the inclination i, the secondary temperature $T_{\rm WD}$, the scaled radii of both

Table 2
Summary of Atmospheric Parameter PTF1 J0823

Telescope	$T_{\rm eff}$ (K) (K)	$\log g$	$\log y$	$v_{\rm rot} \sin i$ (km s^{-1})
DBSP	26,700 ± 600	5.49 ± 0.06	−2.47[a]	132[a]
ISIS	27,100 ± 500	5.50 ± 0.05	−2.47[a]	122 ± 21
HIRES	27,100[b]	5.50[b]	−2.47 ± 0.03	132 ± 5
adopted	27,100 ± 500	5.50 ± 0.05	−2.47 ± 0.03	132 ± 5

Notes.
[a] Fixed to the values derived from HIRES.
[b] Fixed to the values derived from ISIS.

Table 3
Overview of the Derived Parameter for PTF1 J0823

Right ascension	R.A. [hours]	08:23:40.04
Declination	Decl. [°]	+08:19:36.5
Visual magnitude[a]	m_V	14.681 ± 0.051
Atmospheric parameter of the sdB		
Effective temperature	$T_{\rm eff}$ [K]	27100 ± 500
Surface gravity	$\log g$	5.50 ± 0.05
Helium abundance	$\log y$	−1.47 ± 0.03
Projected rotational velocity	$v_{\rm rot} \sin i$ [km s^{-1}]	132 ± 5
Orbital parameter		
	T_0 [BJD UTC]	57418.6202(2)
Orbital period	$P_{\rm orb}$ [minutes]	87.49668(1)
RV semi-amplitude	K [km s^{-1}]	211.7 ± 1.8
System velocity	γ [km s^{-1}]	33.3 ± 1.4
Binary mass function	$f_{\rm m}$ [$M_\odot$]	0.0597 ± 0.0020
Derived parameter		
Mass ratio	$q = \frac{M_{\rm WD}}{M_{\rm sdB}}$	$1.03^{+0.10}_{-0.08}$
sdB mass	$M_{\rm sdB}$ [$M_\odot$]	$0.45^{+0.09}_{-0.07}$
sdB radius	$R_{\rm sdB}$ [$R_\odot$]	$0.20^{+0.03}_{-0.02}$
WD mass	$M_{\rm WD}$ [$M_\odot$]	$0.46^{+0.12}_{-0.09}$
Orbital inclination	i [°]	52^{+8}_{-7}
Separation	a [$R_\odot$]	$0.63^{+0.05}_{-0.04}$
Distance	d [kpc]	$1.2^{+0.2}_{-0.2}$
Derived parameter assuming the canonical sdB mass		
Mass ratio	$q = \frac{M_{\rm WD}}{M_{\rm sdB}}$	$1.04^{+0.10}_{-0.08}$
sdB mass	$M_{\rm sdB}$ [$M_\odot$]	0.47 (fixed)
sdB radius	$R_{\rm sdB}$ [$R_\odot$]	$0.204^{+0.007}_{-0.006}$
WD mass	$M_{\rm WD}$ [$M_\odot$]	$0.49^{+0.05}_{-0.04}$
Orbital inclination	i [°]	51^{+4}_{-4}
Separation	a [$R_\odot$]	$0.641^{+0.010}_{-0.009}$
Distance	d [kpc]	$1.2^{+0.1}_{-0.1}$

Note.
[a] Taken from the APASS catalog (Henden et al. 2016).

components $r_{\rm sdB,WD}$, the velocity scale ($[K + K_{\rm WD}]/\sin i$), and the beaming parameter B ($F_\lambda = F_{0,\lambda}[1 - B\frac{v_r}{c}]$, see Bloemen et al. 2011). Besides these system parameters, we add a third-order polynomial to correct for any residual airmass effects.

To determine the uncertainties on the parameters, we combine `LCURVE` with `emcee` (Foreman-Mackey et al. 2013). `emcee` is an implementation of an MCMC sampler and uses a number of parallel chains to explore the solution space. We use 2048 chains and let them run until the chains stabilized to a solution, which took approximately 6000 generations. Figure 4 shows the ULTRASPEC light curve togehter with the Lcurve fit.

With the surface gravity (g) and projected rotational velocity ($v_{\rm rot} \sin i$), we have three equations at hand that constrain the system, with the sdB mass $M_{\rm sdB}$ the only free parameter. The binary mass function

$$f_{\rm m} = \frac{M_{\rm WD}^3 \sin^3(i)}{(M_{\rm WD} + M_{\rm sdB})^2} = \frac{P_{\rm orb} K^3}{2\pi G} \quad (1)$$

can be combined with

$$\sin i = \frac{(v_{\rm rot} \sin i) P_{\rm orb}}{2\pi R_{\rm sdB}} \quad (2)$$

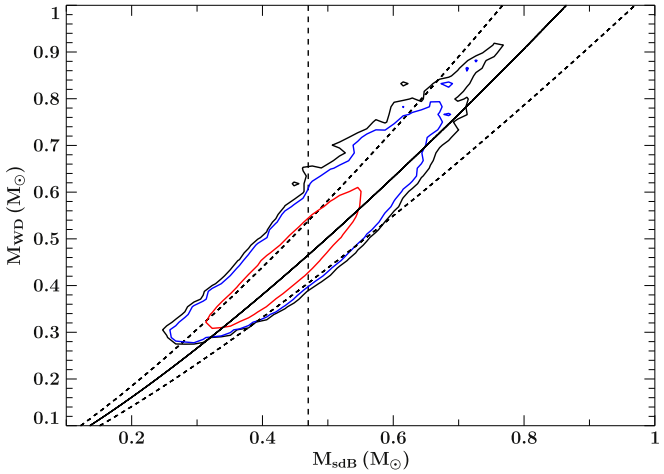

Figure 5. White dwarf mass vs. sdB mass. The curved lines correspond to synchronization with the corresponding error. The dashed vertical line marks the canonical sdB mass of 0.47 $M_\odot$. The contours show the results from the light-curve fit with 1σ (red), 2σ (blue), and 3σ (black) confidence.

and

$$R_{\rm sdB} = \sqrt{\frac{M_{\rm sdB} G}{g}} \quad (3)$$

with $P_{\rm orb}$ being the orbital period, K the velocity semi-amplitude, $M_{\rm WD}$ the mass of the companion, and $R_{\rm sdB}$ the radius of the sdB. The approach is described in full detail in Geier et al. (2007). A strict lower mass limit for the sdB can be derived, because the inclination cannot exceed 90°. We found a lower limit for the sdB mass $M_{\rm sdB} > 0.25\ M_\odot$. The error is dominated by the surface gravity, which has to be estimated from the model atmosphere fit.

5. System Parameters

Because the system is not eclipsing, we cannot obtain a unique solution for the component masses from the light-curve analysis. In order to determine masses and radii of both the sdB and the WD companion, we combined the results from the light-curve analysis with the assumption of tidal synchronization of the sdB primary to the orbit. The given errors are all 95% confidence limits.

We find that both components have nearly the same mass. A mass ratio of $q = M_{\rm WD}/M_{\rm sdB} = 1.03^{+0.10}_{-0.08}$, a mass for the sdB of $M_{\rm sdB} = 0.45^{+0.09}_{-0.07}\ M_\odot$, and a WD companion mass of $M_{\rm WD} = 0.46^{+0.12}_{-0.09}\ M_\odot$ were derived (Figure 5). The inclination is found to be $i = 52^{+8}_{-7}$° (Figure 6). The beaming factor is $B = 1.3^{+0.4}_{-0.4}$, which is consistent with the theoretical value 1.74 (for an sdB with $T_{\rm eff} = 27{,}100$, $\log g = 5.50$). Because the system is not eclipsing, the radius and temperature of the white dwarf are poorly constrained.

The distance to PTF1 J0823 was calculated using the visual V magnitude (m_V), the sdB mass, $T_{\rm eff}$, and $\log g$ as described in Ramspeck et al. (2001). We find a distance to PTF1 J0823 of $d = 1.2^{+0.2}_{-0.2}$ kpc.

An overview of the derived system parameter is given in Table 3.

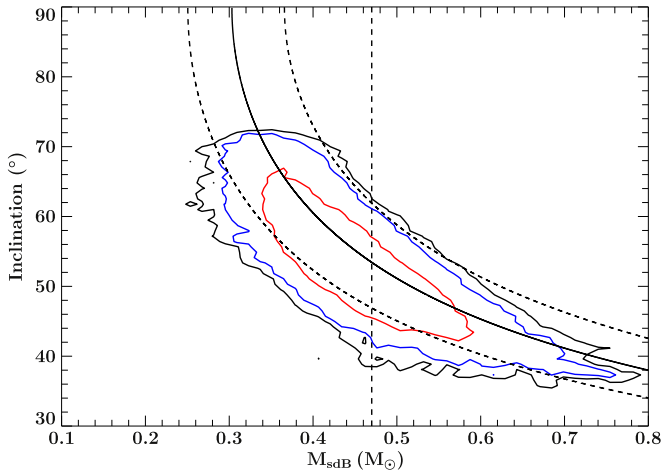

Figure 6. Inclination vs. sdB mass. The curved lines correspond to synchronization with the corresponding error. The dashed vertical line marks the canonical sdB mass of 0.47 $M_\odot$. The contours show the results from the light-curve fit with 1σ (red), 2σ (blue), and 3σ (black) confidence.

6. Discussion

6.1. Evolutionary History

In the standard scenario, the so-called second CE channel, the system starts as a low-mass binary with $\approx$1 $M_\odot$ components. The initially more massive star first evolves to become a WD. Subsequently, the sdB progenitor fills its Roche lobe at the tip of the red-giant branch (RGB), forming an sdB with a canonical mass of $M_{\rm WD} = 0.47\ M_\odot$, set by the helium core flash, with a WD companion (Han et al. 2002, 2003). Han et al. (2002) showed that the binding energy of the envelope is very small at the tip of the RGB for a 1 $M_\odot$ star and therefore the orbital shrinkage in the CE phase is not significant. They predict that sdB+WD binaries are formed with orbital periods longer than those found in PTF1 J0823.

In a different picture an ultracompact sdB+WD binary can also be formed from a more massive main-sequence binary, where the sdB progenitor is $>2M_\odot$. This sdB progenitor ignites helium non-degenerately in the core and fills its Roche lobe during the Hertzsprung gap or at the base of the RGB, resulting in an sdB with either a lower or higher mass compared to the tip of the RGB (Nelemans 2010; Geier et al. 2013). In such systems, the envelope is more tightly bound and the orbital shrinkage required to eject the CE becomes higher (Nelemans 2010; Geier et al. 2013). Geier et al. (2013) showed that CD-30° 11223 evolved most likely from a 2 $M_\odot$ progenitor for the sdB with a 3–4 $M_\odot$ companion for the WD progenitor. The WD companion in PTF1 J0823 is, with an upper mass limit of $M_{\rm WD} = 0.58\ M_\odot$, less massive than in CD-30° 11223.

Perhaps the most similar system is KPD 0422+5421 (Koen et al. 1998). However, its orbital period is $P_{\rm orb} = 129.6$ minutes and therefore about 42 minutes longer than PTF1 J0823. Due to the longer period in KPD 0422+5421, this system is easier to explain by the second CE channel from Han et al. (2002).

6.2. Future Evolution

To understand the future evolution of the system, we used the code MESA (Paxton et al. 2011, 2013, 2015). For the model, we assumed an sdB with a canonical mass of $M_{\rm sdB} = 0.47\ M_\odot$ with a white dwarf companion of $M_{\rm WD} = 0.49\ M_\odot$. Using release version 8118, we construct

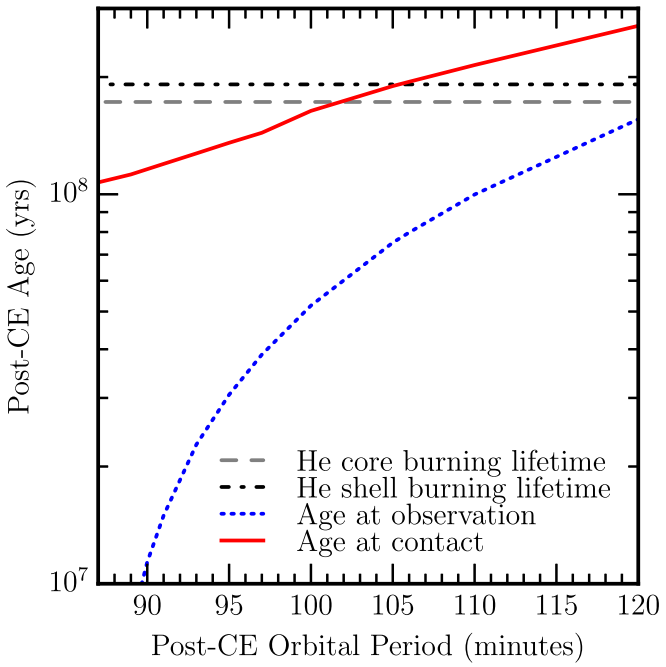

Figure 7. Model post-CE orbital period is shown on the x-axis, with the post-CE age on the y-axis. The dashed gray and dashed–dotted black lines show the core and shell He burning lifetimes of the sdB, respectively. The dotted blue curve shows the ages of the models when the orbital period matches the period that we observed for this system. The red curve shows the ages at which the stars make contact. Systems with initial orbital periods longer than 106 minutes will make contact after the sdB finishes He burning.

binary simulations that model the full stellar structure equations for the sdB and treat the WD as a point mass. We ran a set of simulations with periods, when the system exits the CE (post-CE orbital period), ranging from 87 to 120 minutes. The evolution of the system is governed by the loss of angular momentum due to radiation of gravitational waves. We record the post-CE age at which the orbital periods match the observed period of 87 minutes, shown by the dotted blue curve in Figure 7, and the age at which the stars make contact, shown by the dashed–dotted red curve. Recent modeling of asteroseismic observations of sdB stars (Constantino et al. 2015) points to convective cores much larger than those found with the Schwarzschild condition. At present, there is no clear consensus on the physics needed to achieve these larger cores, which prolongs the lifetime of the He burning phase. To accommodate such an outcome, we performed runs with element diffusion active (Michaud et al. 2007; Schindler et al. 2015), doubling the convective core mass (from 0.109 $M_\odot$ to 0.218 $M_\odot$) and the core-burning lifetime (from 80 to 152 Myr). The data from these runs are shown in Figures 7 and 8.

If contact is made after core and shell He burning have finished (dashed gray and dashed–dotted black curves in Figure 7) and the sdB has become a C/O WD with a 0.41 $M_\odot$ core and 0.06 $M_\odot$ He envelope, the component that used to be the sdB will overflow its Roche lobe at an orbital period of less than 2 minutes, leading to a prompt merger and formation of an R CrB-type star and subsequent evolution into a massive single WD. Figure 7 shows that the post-CE orbital period lower limit for this outcome is 106 minutes.

On the other hand, if the post-CE orbital period is less than 106 minutes, contact is made during the He burning phase, a

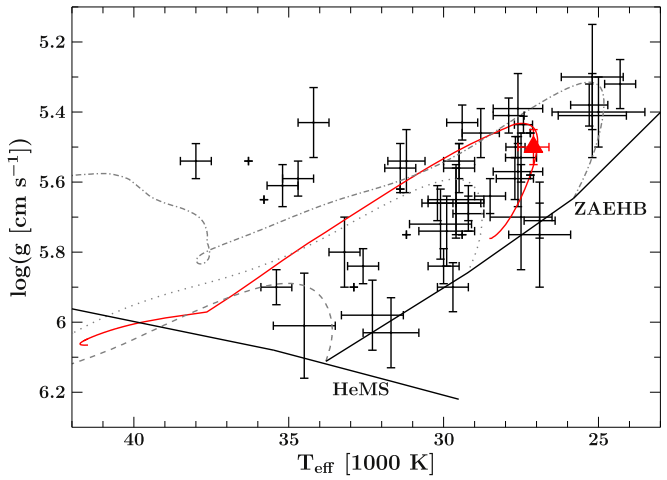

Figure 8. $T_{\rm eff}$–log g diagram of the compact binary sdB stars with confirmed white dwarf companions (Kupfer et al. 2015). The red triangle marks PTF1 J0823. The helium main sequence (HeMS), the zero-age EHB (ZAEHB), and the terminal-age EHB (TAEHB) are superimposed with EHB evolutionary tracks by Han et al. (2002; dashed lines: $m_{\rm env} = 0.000\ M_\odot$, dotted lines: $m_{\rm env} = 0.001\ M_\odot$, dashed–dotted lines: $m_{\rm env} = 0.005\ M_\odot$ using $0.45\ M_\odot$ models). The red solid line shows the EHB evolutionary track calculated with MESA using a $0.47\ M_\odot$ model with $m_{\rm env} = 5 \times 10^{-4}\ M_\odot$.

merger may be avoided and the sdB will donate its remaining helium in an AM CVn-type system (Brooks et al. 2015).

6.3. Current Age

Figure 8 shows the position of PTF1 J0823 in the $T_{\rm eff}$–log g diagram overplotted with the confirmed sdB+white dwarf systems in compact orbits as well as theoretical evolutionary tracks. The sdBs with WD companions populate the full extreme horizontal branch (EHB) band homogeneously with a small fraction of sdBs having evolved off the EHB. The values of $T_{\rm eff}$ and log g for PTF1 J0823 are consistent with an sdB on the EHB in the core helium burning stage.

In a comparison of the spectroscopically derived $T_{\rm eff}$ and log g with our MESA models, we find that an sdB model with a $5 \times 10^{-4}\ M_\odot$ hydrogen envelope matches the atmospheric parameter at a post-CE age of 94 Myr (Figure 8), corresponding to a post-CE orbital period of 109 minutes, which is close to the limit where the sdB still burns helium when filling its Roche lobe.

7. Conclusion and Summary

Motivated by the possible existence of detached hot (ultra-) compact binaries such as CD−30° 11223, PTF1 J0823 was found in a cross-match between an SDSS color selected sample and the PTF database.

The P48 light curve of PTF1 J0823, with a baseline of more than five years, revealed ellipsoidal deformation of the sdB. An orbital period of $P_{\rm orb} = 87.49668(1)$ minutes was found, which makes PTF1 J0823 the second-most compact sdB system known so far. Although the system is not eclipsing, we have been able to derive a mass for the sdB of $M_{\rm sdB} = 0.45^{+0.09}_{-0.07}\ M_\odot$ and WD companion mass of $M_{\rm WD} = 0.46^{+0.12}_{-0.09}\ M_\odot$ by assuming a tidally locked sdB. The distance was found to be $d = 1.2^{+0.2}_{-0.2}$ kpc.

Although the solution allows for a wide range of companion masses, we can exclude a massive white dwarf in PTF1 J0823: $M_{\rm WD} < 0.58\ M_\odot$. The upper limit on the WD mass is only possible if the sdB is also on the upper limit of its mass range with $M_{\rm sdB} \approx 0.54\ M_\odot$, which is not excluded, though only possible if the system evolved from a more massive binary system with main-sequence components $>2\ M_\odot$. If the sdB has a canonical mass of $0.47\ M_\odot$, the companion is a low-mass white dwarf with a mass of $0.45 < M_{\rm WD} < 0.54\ M_\odot$.

Kupfer et al. (2015) found that a significant fraction of the sdB binaries host WDs of masses below $0.6\ M_\odot$, but all have longer periods of at least a few hours. Therefore, PTF1 J0823 is the first sdB with a confirmed low-mass white dwarf companion in a tight orbit.

We calculated the evolutionary history of PTF1 J0823 using MESA, assuming a canonical sdB mass ($M_{\rm sdB} = 0.47 M_\odot$), and a companion mass of $M_{\rm WD} = 0.49\ M_\odot$. We found that the sdB will burn helium for 152 Myr and such a system will start accretion while the sdB is still burning helium if the orbital period after the system left the CE was smaller than 106 minutes.

If the system reaches contact after the helium burning has finished, the most likely outcome is a double white dwarf merger and subsequent evolution into an R CrB star with a mass of 0.8–0.9 $M_\odot$, which is the most common mass range for R CrB stars (Saio 2008; Clayton 2012). The final evolutionary stage will be a single massive WD.

However, if the sdB still burns helium when the system reaches contact, the sdB starts to accrete helium-rich material onto the WD companion and the most likely outcome is a helium accreting AM CVn-type system. Therefore, compact sdB binaries with WD companions and post-CE orbital periods $\lesssim$100 minutes might contribute to the population of AM CVn binaries with helium star donors.

Whether PTF1 J0823 is an R CrB progenitor or whether a merger is prevented and the system forms an AM CVn-type system remains elusive and requires more detailed evolutionary calculations as well as more accurate mass measurements, which will be available through Gaia photometry and parallaxes.

This work was supported by the GROWTH project funded by the National Science Foundation under Grant No 1545949. J.v.R. acknowledges support by the Netherlands Research School of Astronomy (NOVA) and the foundation for Fundamental Research on Matter (FOM). T.R.M. acknowledges the support from the Science and Technology Facilities Council (STFC), ST/L00733. This research was partially funded by the Gordon and Betty Moore Foundation through Grant GBMF5076 to Lars Bildsten. This work was supported by the National Science Foundation under grants PHY 11-25915, AST 11-09174, and AST 12-05574. This work was supported in part by the National Science Foundation under Grant No. PHYS-1066293 and the hospitality of the Aspen Center for Physics where parts of this paper was written. We thank the referee for helpful and timely comments.

Observations were obtained with the Samuel Oschin Telescope at the Palomar Observatory as part of the PTF project, a scientific collaboration between the California Institute of Technology, Columbia University, Las Cumbres Observatory, the Lawrence Berkeley National Laboratory, the National Energy Research Scientific Computing Center, the University of Oxford, and the Weizmann Institute of Science. Some of the data presented herein were obtained at the W.M. Keck Observatory, which is operated as a scientific partnership among the California Institute of Technology, the University of

California and the National Aeronautics and Space Administration. The Observatory was made possible by the generous financial support of the W.M. Keck Foundation. The authors wish to recognize and acknowledge the very significant cultural role and reverence that the summit of Mauna Kea has always had within the indigenous Hawaiian community. We are most fortunate to have the opportunity to conduct observations from this mountain. Some results presented in this paper are based on observations made with the WHT operated on the island of La Palma by the Isaac Newton Group in the Spanish Observatorio del Roque de los Muchachos of the Institutio de Astrofisica de Canarias.

Software: `PyRAF` (Bellm & Sesar 2016), `MAKEE` (http://www.astro.caltech.edu/tb/ipac_staff/tab/makee/), `Gatspy` (VanderPlas & Ivezić 2015), `LCURVE` (Copperwheat et al. 2010), `emcee` (Foreman-Mackey et al. 2013), `MESA` (Paxton et al. 2011, 2013, 2015), `FITSB2` (Napiwotzki et al. 2004).

References

Bellm, E. C., & Sesar, B. 2016, pyraf-dbsp: Reduction Pipeline for the Palomar Double Beam Spectrograph, Astrophysics Source Code Library, ascl:1602.002
Bildsten, L., Shen, K. J., Weinberg, N. N., & Nelemans, G. 2007, ApJL, 662, L95
Bloemen, S., Marsh, T. R., Østensen, R. H., et al. 2011, MNRAS, 410, 1787
Brooks, J., Bildsten, L., Marchant, P., & Paxton, B. 2015, ApJ, 807, 74
Carter, D., Benn, C. R., Rutten, R. G. M., et al. 1993, ISIS User's Manual, http://www.ing.iac.es/astronomy/observing/manuals/ps/wht_instr/isis_users.pdf
Claret, A. 2004, A&A, 428, 1001
Clayton, G. C. 2012, JAVSO, 40, 539
Constantino, T., Campbell, S. W., Christensen-Dalsgaard, J., Lattanzio, J. C., & Stello, D. 2015, MNRAS, 452, 123
Copperwheat, C. M., Marsh, T. R., Dhillon, V. S., et al. 2010, MNRAS, 402, 1824
Dhillon, V. S., Marsh, T. R., Atkinson, D. C., et al. 2014, MNRAS, 444, 4009
Dhillon, V. S., Marsh, T. R., Stevenson, M. J., et al. 2007, MNRAS, 378, 825
Fink, M., Röpke, F. K., Hillebrandt, W., et al. 2010, A&A, 514, A53
Foreman-Mackey, D., Hogg, D. W., Lang, D., & Goodman, J. 2013, PASP, 125, 306
Geier, S., Hirsch, H., Tillich, A., et al. 2011, A&A, 530, A28
Geier, S., Marsh, T. R., Wang, B., et al. 2013, A&A, 554, A54
Geier, S., Nesslinger, S., Heber, U., et al. 2007, A&A, 464, 299
Han, Z., Podsiadlowski, P., Maxted, P. F. L., & Marsh, T. R. 2003, MNRAS, 341, 669
Han, Z., Podsiadlowski, P., Maxted, P. F. L., Marsh, T. R., & Ivanova, N. 2002, MNRAS, 336, 449
Heber, U. 1986, A&A, 155, 33
Heber, U. 2009, ARA&A, 47, 211
Heber, U. 2016, PASP, 128, 082001
Heber, U., Reid, I. N., & Werner, K. 2000, A&A, 363, 198
Henden, A. A., Templeton, M., Terrell, D., et al. 2016, yCat, 2336
Iben, I., Jr., & Tutukov, A. V. 1991, ApJ, 370, 615
Koen, C., Orosz, J. A., & Wade, R. A. 1998, MNRAS, 300, 695
Kupfer, T., Geier, S., Heber, U., et al. 2015, A&A, 576, A44
Laher, R. R., Surace, J., Grillmair, C. J., et al. 2014, PASP, 126, 674
Law, N. M., Kulkarni, S. R., Dekany, R. G., et al. 2009, PASP, 121, 1395
Livne, E. 1990, ApJL, 354, L53
Livne, E., & Arnett, D. 1995, ApJ, 452, 62
Maxted, P. f. L., Heber, U., Marsh, T. R., & North, R. C. 2001, MNRAS, 326, 1391
Michaud, G., Richer, J., & Richard, O. 2007, ApJ, 670, 1178
Napiwotzki, R., Karl, C. A., Lisker, T., et al. 2004, Ap&SS, 291, 321
Nelemans, G. 2010, Ap&SS, 329, 25
Ofek, E. O., Laher, R., Law, N., et al. 2012, PASP, 124, 62
Oke, J. B., & Gunn, J. E. 1982, PASP, 94, 586
Paxton, B., Bildsten, L., Dotter, A., et al. 2011, ApJS, 192, 3
Paxton, B., Cantiello, M., Arras, P., et al. 2013, ApJS, 208, 4
Paxton, B., Marchant, P., Schwab, J., et al. 2015, ApJS, 220, 15
Piersanti, L., Tornambé, A., & Yungelson, L. R. 2014, MNRAS, 445, 3239
Ramspeck, M., Heber, U., & Edelmann, H. 2001, A&A, 379, 235
Rau, A., Kulkarni, S. R., Law, N. M., et al. 2009, PASP, 121, 1334
Saio, H. 2008, in ASP Conf. Ser. 391, Hydrogen-Deficient Stars, ed. A. Werner & T. Rauch (San Francisco, CA: ASP), 69
Savonije, G. J., de Kool, M., & van den Heuvel, E. P. J. 1986, A&A, 155, 51
Schindler, J.-T., Green, E. M., & Arnett, W. D. 2015, ApJ, 806, 178
Shakura, N. I., & Postnov, K. A. 1987, A&A, 183, L21
Shen, K. J., & Bildsten, L. 2014, ApJ, 785, 61
Tutukov, A. V., & Fedorova, A. V. 1989, SvA, 33, 606
Tutukov, A. V., & Yungelson, L. R. 1990, SvA, 34, 57
VanderPlas, J. T., & Ivezić, V. 2015, ApJ, 812, 18
Vennes, S., Kawka, A., O'Toole, S. J., Németh, P., & Burton, D. 2012, ApJL, 759, L25
Verbunt, F., & Rappaport, S. 1988, ApJ, 332, 193
von Zeipel, H. 1924, MNRAS, 84, 665
Wang, B., Meng, X., Chen, X., & Han, Z. 2009, MNRAS, 395, 847
Woosley, S. E., & Kasen, D. 2011, ApJ, 734, 38
Yungelson, L. R. 2008, AstL, 34, 620